MBE Growth and Structural and Electrochemical Characterization of Tin Oxide and Indium Tin Oxide Nanoparticles Grown on Silicon for Li-ion Battery Anodes

Michal J. Osiak[1], Eileen Armstrong[1], Tadhg Kennedy[2,3], Clivia M. Sotomayor Torres[4,5,6], Kevin M. Ryan[2,3], and Colm O'Dwyer[1,3,7]

[1] *Department of Chemistry, University College Cork, Cork, Ireland*
[2] *Department of Chemical and Environmental Sciences, University of Limerick, Limerick, Ireland*
[3] *Materials & Surface Science Institute, University of Limerick, Limerick, Ireland*
[4] *Catalan Institute of Nanotechnology, Campus UAB, Edifici CM3, Bellaterra, 08193 (Barcelona) Spain*
[5] *Catalan Institute for Research and Advances Studies (ICREA), 08010 Barcelona, Spain*
[6] *Department of Physics, Universidad Autonoma de Barcelona, Campus UAB, 08193 Bellaterra, Spain*
[7] *Micro & Nanoelectronics Centre, Tyndall National Institute, Dyke Parade, Cork, Ireland*

Tin oxide (SnO_2) is considered a very promising material as a high capacity Li-ion battery anode. Typically, the electrochemical performance of tin oxide based anodes is dependent on various factors such as their size and composition. Here, we demonstrate how defined dispersion of nanostructures can improve the understanding of the relationship between the electrode performance and its architecture. Two different types of well-defined hierarchical $Sn@SnO_2$ core-shell nanoparticle dispersions were prepared by molecular beam epitaxy (MBE) on silicon, composed of either amorphous or polycrystalline SnO_2 shells. Sn doped In_2O_3 (ITO) NP dispersions are also demonstrated from MBE nanoparticle growth. Preparation of SnO_2 and related materials by highly defined MBE growth as a model system allows a detailed examination of the influence of material dispersion or nanoarchitecture on the performance of active electrode materials.

Introduction

Lithium-ion batteries are widely used today in portable electronics, telecommunication and medical devices. Li-ion technologies are rechargeable and offer advantages such as high energy density, lack of unwanted memory effects and relatively long cycle lifetimes (1-4). Batteries with better rate performance, higher capacity and increased safety are required for advanced applications and to satisfy consumer demands for portable electronic devices with greater power and energy requirements. (5, 6). However, current battery anodes made from layered graphitic carbon are limited by a theoretical capacity of 372 mAh g^{-1} (7), which limits the overall cell capacity when paired with a high capacity cathode material.

Considerable research is therefore being directed to the study of emerging alternative anode materials with higher capacities such as Sn (990 mAh g^{-1}) (8), SnO (876 mAh g^{-1}), SnO_2 (780 mAh g^{-1}) (7, 9-14), Sb (660 mAh g^{-1}) (15), Si (4200 mAh g^{-1}) (16) and Ge (1600 mAh g^{-1}) (17). SnO_2 in particular is receiving renewed interest due to simplicity of synthesis and reports of improving performance (7, 13, 18-20). However, SnO_2 (like all the materials listed above) undergoes drastic volume changes (~200%) upon electrochemical alloying with lithium (21). These changes may cause capacity loss and poor cycle life, which originate from loss of

electrical contact between the active material and current collector as well from decrease of electrode penetration of the agglomerated active material (22).

Effective strategies have been proposed to resolve issues arising in SnO_2 based Li-ion battery anodes. Synthesis of nanoscale SnO_2 with porous, layered, or multiphasic structures, such as nanosheets (23, 24), nanotubes (24, 25) and core-shell nanostructures (26, 27) have been investigated. These types of structures allow for a high density of materials with small diffusion lengths which improves Li^+ insertion rates (28). As an alternative, various composites have been proven to be more effective in enhancing the stability of SnO_2 based electrodes (29, 30). Solvothermal and hydrothermal and microwave processes (31, 32), plasma jet reactor synthesis (33), AAO assisted etching (34) and various other templating methods (35-38) were extensively used to prepare nanorods, nanoplates, nanowires, and core-shell particles of SnO_2. A number of composite structures (such as CNT-SnO_2 or Fe_3O_4/SnO_2) (39, 40) were also developed that demonstrated a large influence of their composite morphology and chemistry on the performance as an anode (41-44). More investigation is needed to understand the changes occurring at the interface between the active materials and their interference with current collector, especially in the situation where the current collector can also react with lithium.

In this work, we present the growth of several novel types of Sn@SnO_2 core-shell nanoparticle dispersions prepared by MBE(45) on silicon, and through electron microscopy and spectroscopies, detail their respective behavior in response to lithium alloying as Li-ion battery anodes. Deposition of Sn, In or both and subsequent oxidative crystallization in air results in formation of characteristic size dispersion of core-shell SnO_2 nanoparticles and Sn doped In_2O_3 Detailed structural characterization and electrochemical cycling was carried out to elucidate how the reversible alloying process with Li is inherently dependent on size dispersion, core-shell structure and composition. This work shows the relationship between the crystalline structure and spatial density of nanostructures on electrochemical processes and details the changes associated with Li insertion and removal into a series of core-shell SnO_2 and ITO NPs on silicon.

Experimental

Prior to the deposition, the surface of silicon was cleaned using standard RCA silicon cleaning procedures, detailed elsewhere. For deposition of Sn and In, a custom-built MBE high-vacuum chamber with two high temperature effusion cells for metallic Sn or In targets, combined with an electron beam evaporator was designed in cooperation with MBE Komponenten GmbH. A uniform layer of Sn metal was deposited at pre-defined rates on a Si(100) substrate at a predefined temperature, and a similar procedure was followed for the co-deposition of Sn and In at 10:90 weight ratio for ITO growth.

Surface morphologies and the chemical composition of the nanostructured dispersions were investigated by scanning electron microscopy (SEM) using a Hitachi SU-70 with an Oxford-50mm^2 X-Max detector for energy dispersive X-ray analysis (EDX). Transmission electron microscopy (TEM) analysis was conducted with a JEOL JEM-2100F field emission microscope operating at 200 kV, equipped with a Gatan Ultrascan CCD camera and EDAX Genesis EDS detector for atomic resolution crystal structure and composition examination. The size distribution of the nanodots was analyzed using ImageJ (46). Cross-sectioning of the SnO_2 nanoparticles formed by MBE was carried out with an FEI Helios Nanolab Dual Beam FIB System.

To investigate the electrochemical insertion (alloying) and removal of Li, cyclic voltammetry measurements were carried out in a 3-electrode setup using a Multi Autolab 101 potentiostat, using Li as both counter and reference electrodes. All potentials, unless otherwise

stated, are relative to Li^+/Li. Swagelok-type cells were used with counter and active material electrode separated by a polypropylene separator soaked in 1 mol dm^{-3} solution of $LiPF_6$ in ethylene carbonate:dimethyl carbonate (EC:DMC) in a 50:50 v/v ratio. The electrodes were potentiodynamically cycled typically at 0.2 mV s^{-1}. Following this, electrodes were washed in acetonitrile and a 10^{-4} mol dm^{-3} solution of acetic acid to remove the electrolyte residue.

Results and discussion

Core-shell $Sn@SnO_2$ nanoparticle dispersions

MBE growth of Sn at elevated temperatures (400^0C-600^0C) and oxidation in air results in the formation of two distinct types of SnO_2 core-shell nanoparticles (NPs) as shown in Fig 1a. The first type of NPs consists of highly crystalline Sn metal core NPs with a thin amorphous coating of SnO_2 (ATO), and the second type comprises a crystalline Sn metal core with a polycrystalline SnO_2 shell (PCTO), forming $Sn@SnO_2$ NPs. Both are formed by simple two step deposition and oxidation mechanism. The SEM image in Fig. 1b shows a dispersion of ATO NPs on the Si substrate. ATO NPs typically have a high size dispersion, ranging from a few nm to over 500 nm in diameter, with an average interparticle distance of ~60 nm, covering about 65% of the sample surface. The NPs are generally close to hemispherical shape, with some deviations probably related to their crystallization process. Small NPs are interspersed between the larger ones indicating that the growth undergoes simultaneous and progressive Sn deposition, surface diffusion of nucleated crystals and coalescence of neighboring particles.

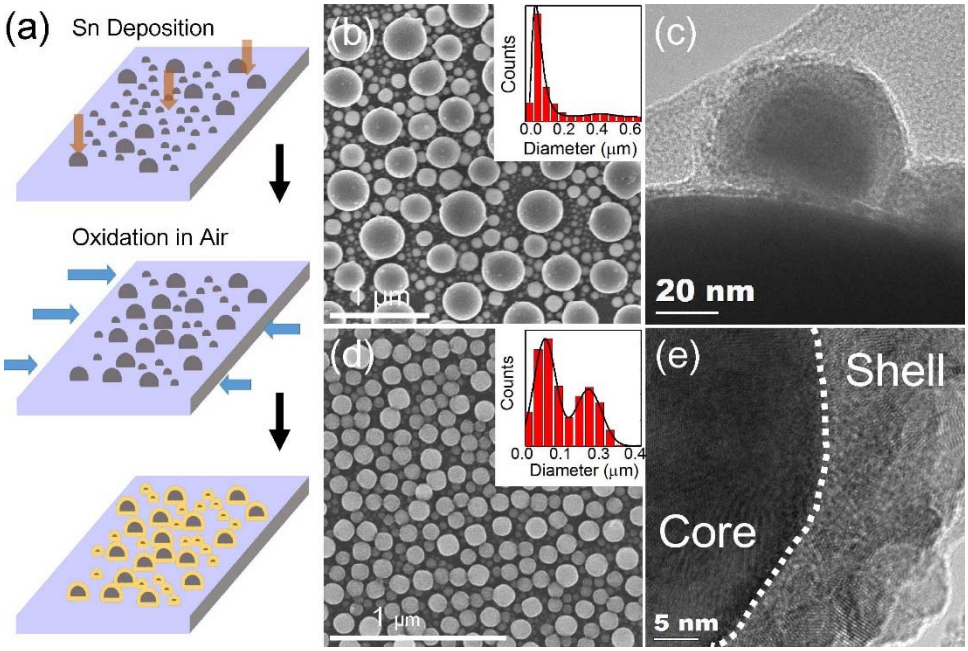

Figure 1. (a) Schematic diagram highlighting steps in formation of core-shell SnO_2 NPs. (b) SEM image showing the ATO NP dispersion. Inset shows the diameter distribution for ATO NPs. (c) TEM image of NPs grown hierarchically on the surface of ATO NP. (d) SEM image of PCTO NP layer. Inset: diameter distribution histogram for PCTO NP layer. (e) TEM image of NPs grown hierarchically on the surface of ATO NP.

The high resolution TEM image in Fig. 1c shows that some of the larger ATO NPs also have smaller NPs growing on their surface. The smaller hierarchical NPs that form on the surface or larger NPs, is believed to occur when the coalescence mechanism that forms larger NPs is interrupted by oxidative crystallization of the liquid-phase Sn droplets on the larger NP

surface. In_2O_3 NPs layers grown by MBE also showed similar hierarchical structure, with additional nanowire growth sometimes found from these crystallite seeds (47). The exact origin of the nanocrystallites on the surface of the ATO NPs is however unclear. Analysis shows a much smaller size dispersion and lower average interparticle distance (~25 nm) for PCTO nanoparticles (Fig. 1d), which is related to lower deposition temperature, allowing particles to form without as much surface diffusion in their liquid state as found for ATO NPs. Compared to the ATO NPs, the PCTO NPs show much lower size dispersion, with the majority of the NPs ~100 nm in diameter (Fig. 1d inset); the total surface coverage is higher than for ATO NPs, amounting to ~80% coverage of the sample surface. High magnification SEM imaging of the NP shows a core-shell structure of the nanoparticle specifically the structure of the polycrystalline shell. The smaller NPs interspersed between larger crystals cover a large portion of the substrate (~30%). The coalescence occurs at slower rate (lower substrate temperature) in case of PCTO NPs resulting in better monodispersity in the surface coverage.

The amorphous layer formed around the crystalline core in ATO NPs can be seen in Fig. 1c. Both amorphous and polycrystalline shells, are formed during oxidative crystallization of the outer layer of the Sn droplet after the deposition. TEM analysis confirms that some of the small crystallites growing on the surface of large ATO particles also exhibit core-shell structure.

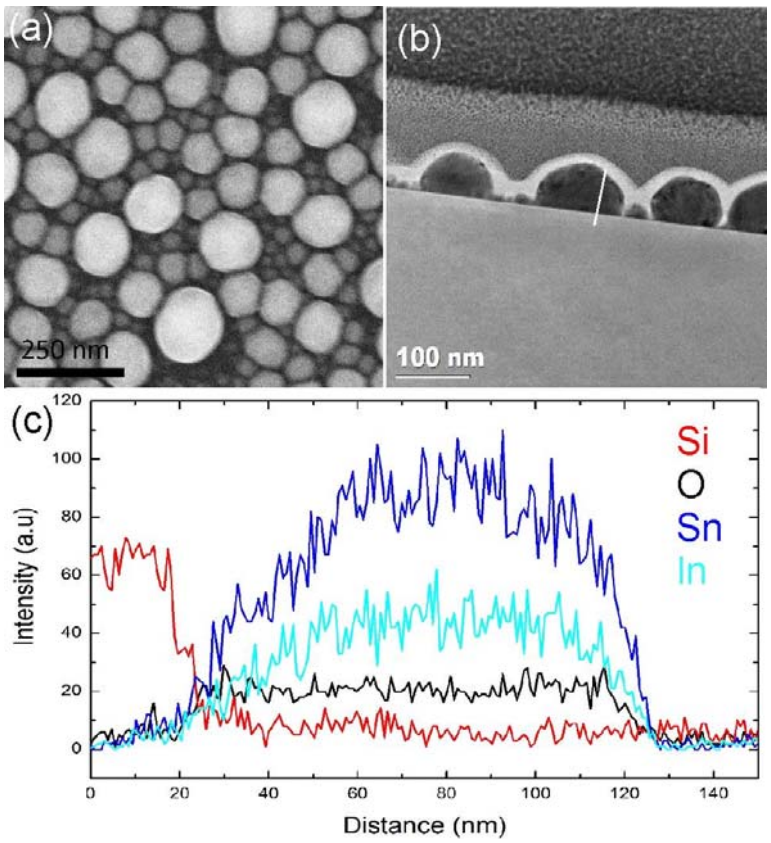

Figure 2. (a) SEM image of an ITO layer. (b) TEM image of a FIB slice of ITO nanoparticles. Line indicates the measurement site for EDX. (c) EDX line spectra for ITO nanoparticles

This hierarchical consistency in core-shell construction indicates that formation of the surface crystallites and NP shells were simultaneous; the thickness of the ATO shell is similar for all particles, despite the 1-2 orders of magnitude difference in core diameter. Moreover, the structure of the crystallites on the surface of ATO is similar to the structure of the PCTO, with a polycrystalline shell around a crystalline core forming a hierarchy of core-shell NPs. The thickness of the amorphous layer is ~10 nm for all NPs on the surface of the substrate or

those on other NPs. The thickness of polycrystalline shell in case of PCTO NPs is of similar order to the ATO NP shell (7-13 nm).

Deposition of Sn and In and subsequent oxidation in air results in formation of crystalline ITO nanoparticles. SEM image of ITO nanoparticle layer is shown in Fig. 2a. The average size of ITO nanoparticles is ~100 nm, which compares to PCTO nanoparticles deposited at the same temperature (400 °C). In case of the ITO nanoparticles, the shell does not form during the deposition, as the nanostructures are prepared in a single step process with oxygen present in the chamber during the deposition. The nanoparticles form with clearly developed crystalline facets, (see Fig. 2b), comparable to In_2O_3 prepared in similar type of deposition (47). Tin atoms, occupying cation sites in cubic bixbyite indium oxide structure act as degenerate dopants, increasing conductivity of the material, which is required for practical applications. The presence of tin in the crystalline structure of the indium oxide was confirmed by energy dispersive spectroscopy (EDX). The linescans are presented in Fig. 2c. A large decrease in the recorded intensity in silicon K_α line is observed at an interface, and increase in measured intensities of Sn, In and O K_α lines are observed.

Reversible lithiation in core-shell SnO_2 NPs

SnO_2 based materials are regarded as promising for Li-ion secondary batteries due to their large theoretical charge storage capacity (29, 48). As the reports on Si-Sn based composite electrodes are limited(49), detailed investigation into electrochemistry and structural changes occurring during lithiation are required. Electrochemical response of a variety of structures, including core-shell SnO_2 NPs, but also comparative In_2O_3 and ITO NP dispersions was investigated by cyclic voltammetry and high resolution electron microscopy. The Li alloying reaction with the Sn NP core is possible if the outer oxide coating can be reduced to Sn^0 from the respective SnO_2 on PCTO and ATO NPs.

Cyclic voltammetry was used to investigate this process. In a CV each alloying, growth, removal, oxidation and reduction process can be examined in each cycle, in the potential window characteristic for each process. This is especially useful in the present case, where numerous processes and several materials are present. The cathodic processes involve the alloying of Li with the reduced form of SnO_2 to form a Li-Sn alloy (charging) and the anodic process follows Li extraction or dealloying (discharging). There is a substantial difference between CVs for ATO (Fig. 3a) and PCTO (Fig. 3b). The large irreversible peak (indicated in the CVs by **I**) is usually regarded as being due to the formation of a stable SEI layer and to electrochemical reduction of SnO_2 to a system of three phases consisting of LiO_2, O_2 and SnO. The formation of an SEI layer (from the voltammetric response) is more pronounced for PCTO samples, which can be attributed to a higher areal mass loading of polycrystalline SnO_2 shell. This reaction is complete at ~1.5 V and is present in both CVs. Subsequently, SnO is reduced to metallic Sn, indicated by large peak present at ~1 V for both systems (**I** for PCTO, **II-III** for ATO). A shift in voltage can be observed in subsequent cycles for PCTO. Two reversible peaks appear in the cathodic scan (**V–VI** for ATO, **V-VII** for PCTO). They occur at potentials that can be attributed to formation of particular Li with Sn: $Li_{2.33}Sn$ formed at 0.55 V and $Li_{4.4}Sn$ is formed at 0.15 V. Oxidation peaks appearing at 0.57 V, 0.81 V, 0.87 V, 0.91 V and 1.21 V correspond to the dealloying of Li_xSn and partially reversible oxidation of Sn to SnO_2. The full set of electrochemical reactions can be described according to (50):

$$Li^+ + e^- + electrolyte \rightarrow SEI \quad (1)$$

$$SnO_2 + 4\,Li^+ + 4e^- \rightarrow Sn + 2\,Li_2O \quad (2)$$

$$Sn + xLi^+ + xe^- \leftrightarrow Li_xSn\ (0 < x < 4.4) \quad (3)$$

The reaction in Eqn. 2, is normally regarded as irreversible. In this case the reduction peak at 1.25 V (**I** for ATO and PCTO NPs) and matching oxidation peak at 1.23 V (**VI** for ATO NPs, **VII** for PCTO NPs) remain stable over the 5 cycles indicating partial reversibility of this reaction compared to bulk SnO_2. Additionally, a small amount of lithium is introduced into the silicon current collector. The insertion and removal potentials for silicon are typically 0.2 V and 0.5 V, respectively. The relatively higher rate of reaction as shown by the larger current in this potential range indicates insertion of lithium into Si coexists with alloying of lithium with Sn.

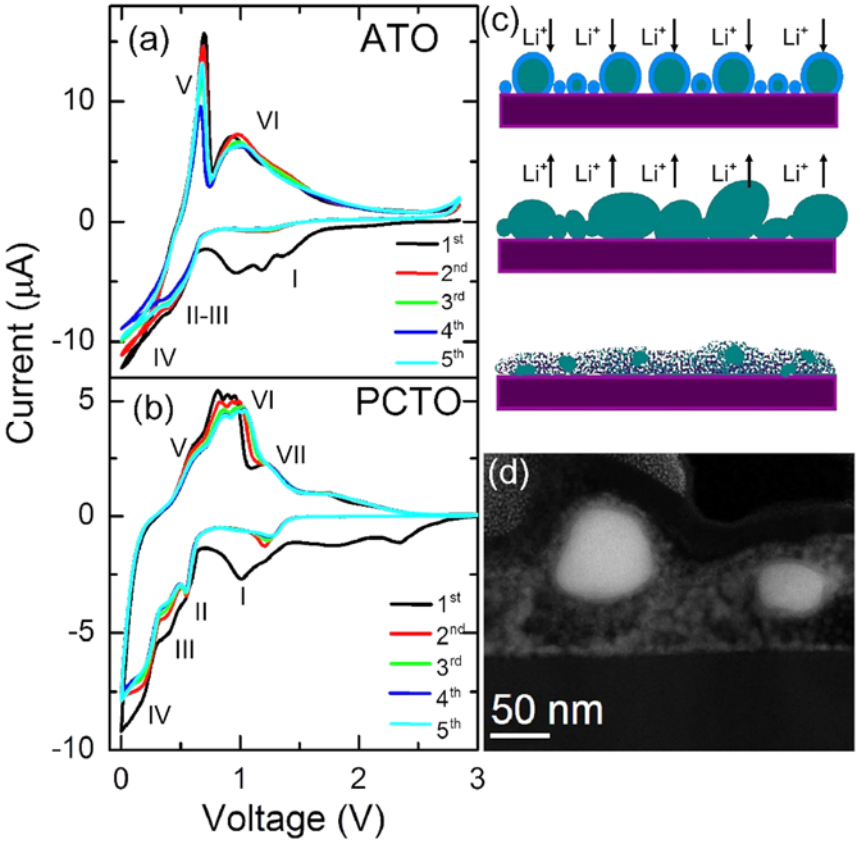

Figure 3. (a) Cyclic voltammograms for ATO and (b) PCTO NPs on silicon. (c) Schematic diagram describing formation of porous NP layers upon lithiation cycling. (d) Dark-field STEM image showing highly porous layer comprising pulverized NPs formed by electrochemical cycling of the PCTO NP layer. The brighter regions are Sn and SnO_2.

For ATO NPs, the large irreversible area in the 1.6-0.8 V range (**I**), corresponds to reduction of SnO_2 to metallic Sn, and the succeeding peak at 0.39 V (**II-III**) corresponds to formation of a Li_xSn phase, where x ranges from $0 < x < 4.4$. This is also found for the PCTO NPs, implying that the crystal structure of the thin shell coatings are less critical than their stoichiometric phases, which are identical. In the lower voltage range corresponding to insertion of lithium into Si, a large peak at ~0.1 V (**IV**) is present. In the anodic part of the CV, two reversible peaks at ~0.65 V (**V**) and ~1 V (**IV**) are found. The first peak, is attributed to the removal of lithium from silicon while the second corresponds to removal of lithium from Sn (51), and it occurs at a similar voltage in both ATO and PCTO core-shell NPs.

The Si insertion and removal rates as indicated by the current in corresponding CV peaks increase with cycling, indicating an activation effect characteristic for Si-based anodes (2, 16, 52-54). Specifically, volumetric expansion of lithiated material causes cracks and exposure of unreacted Si to the electrolyte, which in turn allows more lithium to be incorporated

into material at the same potential. Usually it is considered a negative effect, causing an increasing degree of fracturing and loss of electrical integrity between the active material and the current collector. As it is not the active material, expansion occurs only where the SnO_2 NPs are not present. Comparing the differences between the ATO and PCTO NPs and their spatial density and size dispersion on the Si, ~25% higher rate of lithium insertion into ATO sample is observed, which correlates well with the surface coverage difference between ATO and PCTO

The electrochemical response of NP dispersions was also investigated for a range of NPs prepared by MBE: In addition to core-shell SnO_2, we investigated In_2O_3 and ITO NP dispersions whose CVs and corresponding size dispersions are presented in Fig. 4.

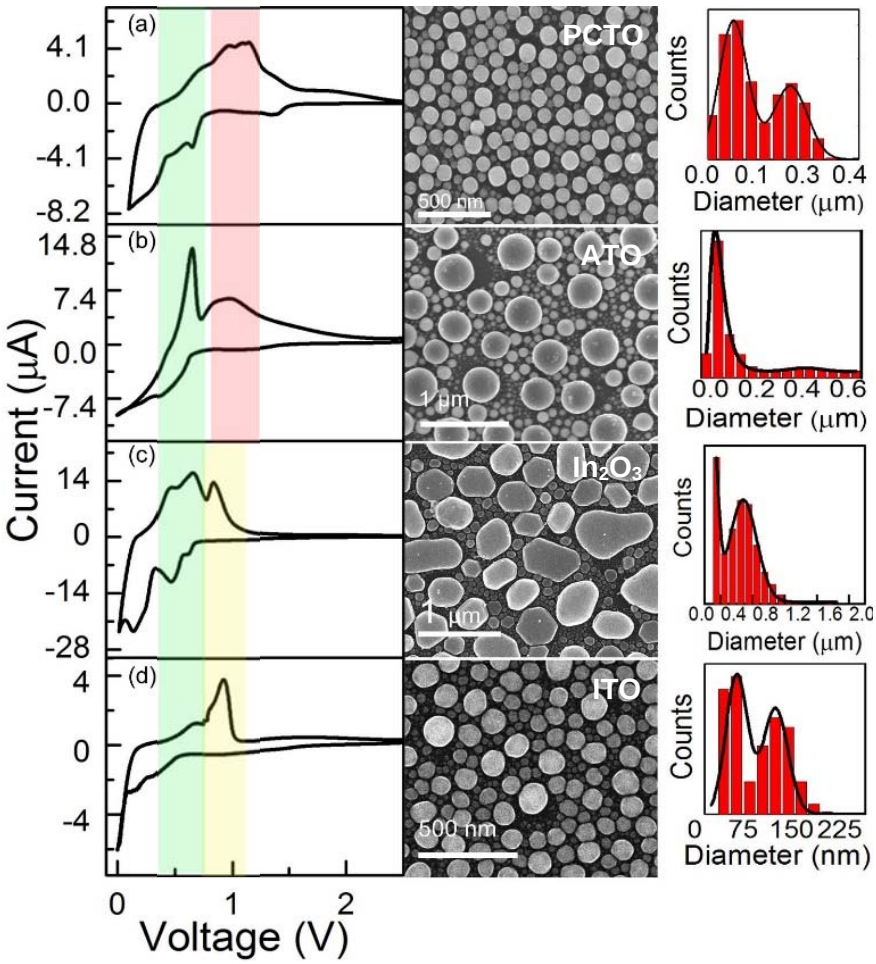

Figure 4. Single cycle voltammograms, SEM image of the surface of the NP layer, and corresponding size dispersion histogram for (a) PCTO NPs, (b) ATO NPs, (c) In_2O_3 NPs, and (d) Sn-doped In_2O_3 (ITO) NPs. De-intercalation potential windows are shaded for Li_xSi (green), Li_xSn (pink) and Li_xIn (yellow).

The cyclic voltammetric response of the various SnO_2 and In_2O_3 NPs dispersions in Fig. 4, show that the lithium insertion and removal characteristics are strongly dependent on the shape and size dispersion of the NPs and their volumetric density; all sample exhibit at least bimodal sizes, with one mode dominating in the case of highly coalesced ATO and In_2O_3 NP dispersions. As all are deposited from In, Sn or In + Sn using MBE, the distributions are characteristics of a similar formation mechanism, outlined earlier for SnO_2. In terms of electrochemical reduction, alloying, intercalation and the reverse processes, there is similarity

between responses for PCTO and ITO NPs (Figs 3a and d), and between ATO NPs and In_2O_3 NP layers (Fig. 4b and c).

Analysis of the data in Fig. 4 shows that both areal density and volumetric density need to be considered, especially when using hybrid systems such as the present case where the current collector (silicon) is capable of intercalating lithium. Lithium insertion and removal peaks for Li_xSi are more pronounced (as measured from the magnitude of the current and integrated charge) for ATO and In_2O_3 NP dispersions, while alloying reactions with active material (In, Sn) dominates for PCTO and ITO NP layers. This trend is due to the areal coverage, whereas the relative contribution of the alloying to intercalation response in these electrodes is linked to the volumetric density of active material. The shape of the voltammetric response in each case thus includes different relative contributions from the CV response of Li-Si formation. For the PCTO and ITO NP dispersions (Figs 3a and d), the Li_xSi phases (*cf.* Fig. 2) are observed, but dominated by the In- and Sn-containing material.

Generally, the dispersion of nanoscale active materials should also consider the diameter or thickness of the active material in addition to the effective porosity, especially in composite systems where insertion or alloying occurs at different potentials via different mechanisms. By varying the dispersion and thus the effective porosity of the active material, hybrid electrodes involving electrochemically active current collectors can also offer some degree of stress-change buffering during deep charging and discharging.

Conclusions

We detailed the MBE growth of two distinct and well defined types of $Sn@SnO_2$ core-shell nanoparticles with crystalline metallic Sn cores and either amorphous or polycrystalline SnO_2 shells. In_2O_3 and Sn doped In_2O_3 (ITO) NP dispersions are also shown using this approach. Electron microscopy and spectroscopy analyses confirmed a hierarchical core-shell structure of the SnO_2 NPs with different diameters to give a range of volumetric and areal densities of material. Lithium alloying with the reduced form of the NPs and co-insertion into the substrate (which also serves as current collector) showed reversible charge storage via alloying with Sn or In. The effect of lithium insertion and removal on different NP dispersions monitored by electron microscopy and cyclic voltammetry, showed that the electrochemical behavior depends on the relative size via the volumetric density of the NPs and their areal dispersion on the surface, in addition to their composition. The compositional and structural engineering on SnO_2 and related materials using highly defined MBE growth as model system has allowed a detailed examination of the influence of material dispersion and nanoarchitecture on the electrochemical performance.

Acknowledgements

MO and EA acknowledge the support of the Irish Research Council under awards RS/2010/2170 and RS/2010/2920. The authors thank Dr Fathima Laffir for assistance in XPS measurements, and Prof. J. D. Holmes for access to the Electron Microscopy Analytical Facility at Tyndall National Institute. COD acknowledges support from Science Foundation Ireland under award no. 07/SK/B1232a, the UCC Strategic Research Fund, and from the Irish Research Council New Foundations Award.

References

1. P. G. Bruce, B. Scrosati and J.-M. Tarascon, *Angew. Chem. Int. Ed.*, **47**, 2930 (2008).
2. Y. G. Guo, J. S. Hu and L. J. Wan, *Adv. Mater.*, **20**, 2878 (2008).
3. H. Li, Z. X. Wang, L. Q. Chen and X. J. Huang, *Adv. Mater.*, **21**, 4593 (2009).

4. L. W. Ji, Z. Lin, M. Alcoutlabi and X. W. Zhang, *Energy Env. Sci.*, **4**, 2682 (2011).
5. J. B. Goodenough and Y. Kim, *J. Power Sources*, **196**, 6688 (2011).
6. J. B. Goodenough and Y. Kim, *Chem. Mater.*, **22**, 587 (2009).
7. J. S. Chen and X. W. Lou, *Small* (2013).
8. M. Winter and J. O. Besenhard, *Electrochim. Acta*, **45**, 31 (1999).
9. A. Sivashanmugam, T. P. Kumar, N. G. Renganathan, S. Gopukumar, M. Wohlfahrt-Mehrens and J. Garche, *J. Power Sources*, **144**, 197 (2005).
10. N. C. Li, C. R. Martin and B. Scrosati, *Electrochem. Solid-State Lett.*, **3**, 316 (2000).
11. M. S. Park, Y. M. Kang, G. X. Wang, S. X. Dou and H. K. Liu, *Adv. Funct. Mater.*, **18**, 455 (2008).
12. G. Zhou, D. W. Wang, L. Li, N. Li, F. Li and H. M. Cheng, *Nanoscale*, **5**, 1576 (2013).
13. J. S. Chen and X. W. Lou, *Mater. Today*, **15**, 246 (2012).
14. M. H. Chen, Z. C. Huang, G. T. Wu, G. M. Zhu, J. K. You and Z. G. Lin, *Mater. Res. Bull.*, **38**, 831 (2003).
15. L. Aldon, A. Garcia, J. Olivier-Fourcade, J.-C. Jumas, F. J. Fernández-Madrigal, P. Lavela, C. P. Vicente and J. L. Tirado, *J. Power Sources*, **119–121**, 585 (2003).
16. U. Kasavajjula, C. Wang and A. J. Appleby, *J. Power Sources*, **163**, 1003 (2007).
17. A. M. Chockla, K. C. Klavetter, C. B. Mullins and B. A. Korgel, *ACS Appl. Mater. Interfaces*, **4**, 4658 (2012).
18. B. Wan, B. Luo, L. Xianlong and L. Zhi, *Mater. Today*, **15**, 544 (2012).
19. C. Wang, Y. Zhou, M. Ge, X. Xu, Z. Zhang and J. Z. Jiang, *J. Am. Chem. Soc.*, **132**, 46 (2009).
20. Y. Chen, J. Ma, Q. Li and T. Wang, *Nanoscale*, **5**, 3262 (2013).
21. R. A. Huggins, *Solid State Ion.*, **113-115**, 57 (1983).
22. H. Li, Q. Wang, L. Shi, L. Chen and X. Huang, *Chem. Mater.*, **14**, 103 (2001).
23. H. Ohgi, T. Maeda, E. Hosono, S. Fujihara and H. Imai, *Cryst. Growth Des.*, **5**, 1079 (2005).
24. Y. Masuda and K. Kato, *J. Crystal Growth*, **311**, 593 (2009).
25. N. Du, H. Zhang, B. Chen, X. Ma and D. Yang, *Chem. Commun.*, **0**, 3028 (2008).
26. X. W. Lou, C. Yuan and L. A. Archer, *Small*, **3**, 261 (2007).
27. H. X. Yang, J. F. Qian, Z. X. Chen, X. P. Ai and Y. L. Cao, *J. Phys. Chem. C*, **111**, 14067 (2007).
28. C. O'Dwyer, V. Lavayen, D. A. Tanner, S. B. Newcomb, E. Benavente, G. Gonzalez, E. Benavente and C. M. S. Torres, *Adv. Funct. Mater.*, **19**, 1736 (2009).
29. I. A. Courtney and J. R. Dahn, *J. Electrochem. Soc.*, **144**, 2045 (1997).
30. J. Fan, T. Wang, C. Z. Yu, B. Tu, Z. Y. Jiang and D. Y. Zhao, *Adv. Mater.*, **16**, 1432 (2004).
31. Y. J. Chen, X. Y. Xue, Y. G. Wang and T. H. Wang, *Appl. Phys. Lett.*, **87**, 233503 (2005).
32. V. Subramanian, W. W. Burke, H. Zhu and B. Wei, *J. Phys. Chem. C*, **112**, 4550 (2008).
33. V. Kumar, J. H. Kim, C. Pendyala, B. Chernomordik and M. K. Sunkara, *J. Phys. Chem. C*, **112**, 17750 (2008).
34. F. Cheng, Z. Tao, J. Liang and J. Chen, *Chem. Mater.*, **20**, 667 (2007).
35. X. W. Lou, Y. Wang, C. Yuan, J. Y. Lee and L. A. Archer, *Adv. Mater.*, **18**, 2325 (2006).
36. Z. Wang, L. Zhou and X. W. Lou, *Adv. Mater.*, **24**, 1903 (2012).
37. S. Ding, J. S. Chen, G. Qi, X. Duan, Z. Wang, E. P. Giannelis, L. A. Archer and X. W. Lou, *J. Am. Chem. Soc.*, **133**, 21 (2010).
38. J. S. Chen, C. M. Li, W. W. Zhou, Q. Y. Yan, L. A. Archer and X. W. Lou, *Nanoscale*, **1**, 280 (2009).

39. Y.-J. Chen, P. Gao, R.-X. Wang, C.-L. Zhu, L.-J. Wang, M.-S. Cao and H.-B. Jin, *J. Phys. Chem. C*, **113**, 10061 (2009).
40. X. W. Lou, J. S. Chen, P. Chen and L. A. Archer, *Chem. Mater*, **21**, 2868 (2009).
41. L. Li, X. Yin, S. Liu, Y. Wang, L. Chen and T. Wang, *Electrochem. Commun.*, **12**, 1383 (2010).
42. Z. Wen, Q. Wang, Q. Zhang and J. Li, *Adv. Funct. Mater.*, **17**, 2772 (2007).
43. G. Cui, Y.-S. Hu, L. Zhi, D. Wu, I. Lieberwirth, J. Maier and K. Müllen, *Small*, **3**, 2066 (2007).
44. M.-S. Park, Y.-M. Kang, S.-X. Dou and H.-K. Liu, *J. Phys. Chem. C*, **112**, 11286 (2008).
45. C. O'Dwyer, M. Szachowicz, G. Visimberga, V. Lavayen, S. B. Newcomb and C. M. S. Torres, *Nat. Nanotech.*, **4**, 239 (2009).
46. C. A. Schneider, Rasband, Wayne S, Eliceiri, Kevin W, *Nat. Methods*, **9** (2012).
47. M. Osiak, W. Khunsin, E. Armstrong, T. Kennedy, C. M. S. Torres, K. M. Ryan and C. O'Dwyer, *Nanotechnology*, **24**, 065401 (2013).
48. H. Inoue, S. Mizutani, H. Ishihara and S. Hatake, *Meeting Abstracts*, **MA2008-02**, 1160 (2008).
49. L. Yan-hong, L. Yua and X.-p. Qiu, *Chinese J. Proc. Eng.*, **11**, 870 (2011).
50. Y. Zhao, J. Li, Y. Ding and L. Guan, *RSC Adv.*, **1**, 852 (2011).
51. M.-S. Park, G.-X. Wang, Y.-M. Kang, D. Wexler, S.-X. Dou and H.-K. Liu, *Angew Chem. Int. Ed.*, **46**, 750 (2007).
52. C. K. Chan, H. Peng, G. Liu, K. McIlwrath, X. F. Zhang, R. A. Huggins and Y. Cui, *Nat. Nanotechnol.*, **3**, 31 (2008).
53. H. Li, X. J. Huang, L. Q. Chen, Z. G. Wu and Y. Liang, *Electrochem. Solid-State Lett.*, **2**, 547 (1999).
54. M. N. Obrovac and L. Christensen, *Electrochem. Solid-State Lett.*, **7**, A93 (2004).